Cell Reports
Methods

Article

# Discontinuity third harmonic generation microscopy for label-free imaging and quantification of intraepidermal nerve fibers

## Graphical abstract

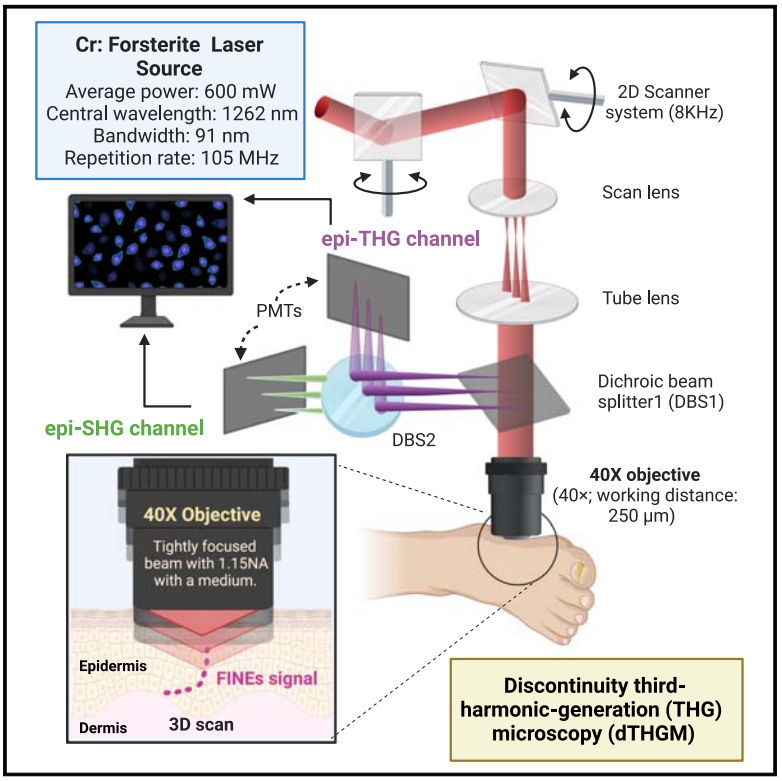


## Highlights

- dTHGM is a methodology for imaging free intraepidermal nerve endings
- Detects 3D discontinuities in third harmonic generation signals as contrast
- dTHGM is a noninvasive and label-free approach
- Provides an intraepidermal nerve fiber (IENF) index to identify small-fiber neuropathy

## Authors

Pei-Jhe Wu, Hsiao-Chieh Tseng, Chi-Chao Chao, ..., Sung-Tsang Hsieh, Wei-Zen Sun, Chi-Kuang Sun

## Correspondence

shsieh@ntu.edu.tw (S.-T.H.), wzsun@ntu.edu.tw (W.-Z.S.), sun@ntu.edu.tw (C.-K.S.)

## In brief

Wu et al. present discontinuity third harmonic generation microscopy (dTHGM), a method that allows for three-dimensional visualization of intraepidermal nerve endings. This label-free, section-free methodology assesses epidermal nerve fibers noninvasively, providing an intraepidermal nerve fiber index for clinical small-fiber neuropathy (SFN) diagnosis. It holds significance for noninvasive SFN diagnosis, including cases of diabetic peripheral neuropathy.

Wu et al., 2024, Cell Reports Methods *4*, 100735
March 25, 2024 
https://doi.org/10.1016/j.crmeth.2024.100735

CellPress

Cell Reports Methods

CellPress
OPEN ACCESS

Article

# Discontinuity third harmonic generation microscopy for label-free imaging and quantification of intraepidermal nerve fibers

Pei-Jhe Wu,[1] Hsiao-Chieh Tseng,[1] Chi-Chao Chao,[2] Yi-Hua Liao,[3] Chen-Tung Yen,[4] Wen-Ying Lin,[4,5] Sung-Tsang Hsieh,[2,7,*] Wei-Zen Sun,[5,7,8,*] and Chi-Kuang Sun[1,6,9,*]

[1]Department of Electrical Engineering and Graduate Institute of Photonics and Optoelectronics, National Taiwan University, Taipei 10617, Taiwan
[2]Department of Neurology, National Taiwan University Hospital, and National Taiwan University College of Medicine, Taipei 100225, Taiwan
[3]Department of Dermatology, National Taiwan University Hospital, and National Taiwan University College of Medicine Taipei 100225, Taiwan
[4]Department of Life Science, National Taiwan University, Taipei 10617, Taiwan
[5]Department of Anesthesiology, National Taiwan University Hospital, and National Taiwan University College of Medicine, Taipei 100225, Taiwan
[6]Graduate Institute of Biomedical Electronics and Bioinformatics and Molecular Imaging Center, National Taiwan University, Taipei 10617, Taiwan
[7]These authors contributed equally
[8]Present address: Department of Anesthesiology, Cathay General Hospital, Taipei 10630, Taiwan
[9]Lead contact
*Correspondence: shsieh@ntu.edu.tw (S.-T.H.), wzsun@ntu.edu.tw (W.-Z.S.), sun@ntu.edu.tw (C.-K.S.)
https://doi.org/10.1016/j.crmeth.2024.100735

**MOTIVATION** Although noninvasive imaging methods enhance our understanding of the human nervous system, they encounter challenges in imaging the discontinuous structure of free intraepidermal nerve endings (FINEs) in human skin. Here, we introduce a clinical imaging methodology, discontinuity third harmonic generation microscopy (dTHGM), which visualizes FINEs in 3D without invasive biopsies and provides an intraepidermal nerve fiber index for clinical evaluation. By using a label-free, section-free technique to examine small nerve fibers in the epidermis, this research provides a valuable tool for healthcare professionals and opens up new possibilities for small-fiber neuropathy diagnosis and treatment assessment.

## SUMMARY

Label-free imaging methodologies for nerve fibers rely on spatial signal continuity to identify fibers and fail to image free intraepidermal nerve endings (FINEs). Here, we present an imaging methodology—called discontinuity third harmonic generation (THG) microscopy (dTHGM)—that detects three-dimensional discontinuities in THG signals as the contrast. We describe the mechanism and design of dTHGM and apply it to reveal the bead-string characteristics of unmyelinated FINEs. We confirmed the label-free capability of dTHGM through a comparison study with the PGP9.5 immunohistochemical staining slides and a longitudinal spared nerve injury study. An intraepidermal nerve fiber (IENF) index based on a discontinuous-dot-connecting algorithm was developed to facilitate clinical applications of dTHGM. A preliminary clinical study confirmed that the IENF index was highly correlated with skin-biopsy-based IENF density (Pearson's correlation coefficient $R = 0.98$) and could achieve differential identification of small-fiber neuropathy ($p = 0.0102$) in patients with diabetic peripheral neuropathy.

## INTRODUCTION

Noninvasive imaging methodologies for nerve fibers are revolutionizing our knowledge of the structure and function of the human nervous system.[1,2] With the development and use of modern imaging techniques, signal continuity of nerve fibers makes it possible to reconstruct the intricate nervous network of the human body.[3,4] MRI has been widely used to identify pathological changes in the CNS and has emerged as the preferred method for studying cranial nerves.[5,6] Diffusion tensor imaging is a novel technique based on MRI that provides superior imaging resolution at the millimeter scale,[7] enabling noninvasive detection of the diffusion of water molecules in the human brain; this diffusion is influenced by the never fiber arrangement, and continuous

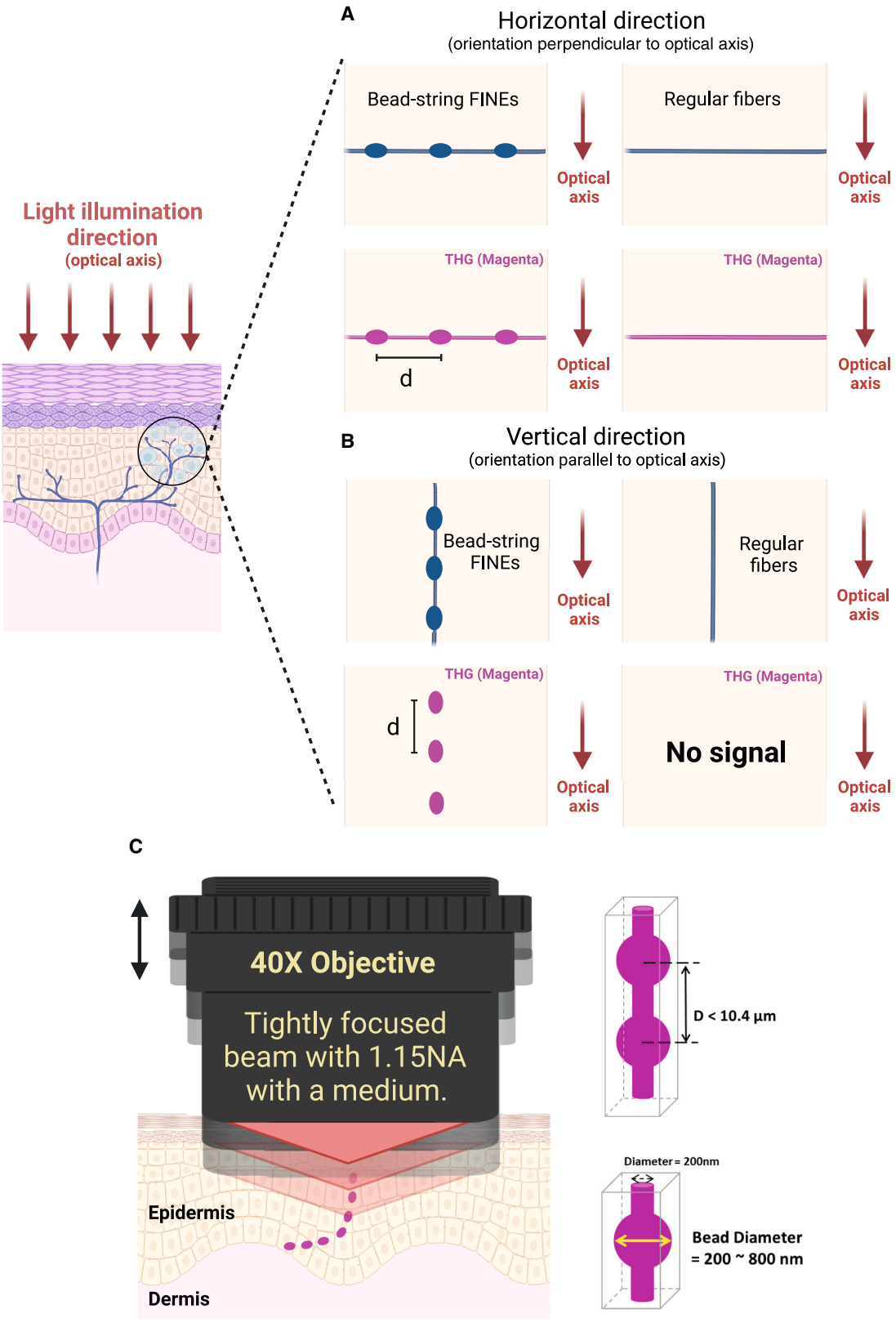


*(legend on next page)*

nerve signals can thus be used to infer the presence of nerve fibers.[2,8] Current high-resolution ultrasound techniques entail using high-frequency sound waves (up to 30 MHz) to create images that enable visualizing submillimeter nerve branches.[2,9] These images provide valuable morphological information on linear nerve structures, and such information can complement nerve conduction studies (NCSs) for identifying possible nerve injury sites and determining the extent of nerve damage.[10] *In vivo* corneal confocal microscopy (CCM) with micron-scale spatial resolution has been used in ophthalmology to examine the continuity of corneal nerve structures.[11] Label-free third harmonic generation (THG) microscopy has high sensitivity to lipids at wavelengths of ~1,180 nm[12] and has thus been applied to image myelinated fibers in mouse brain tissues both *ex vivo* and *in vivo*.[13,14] Studies have verified that THG signals are produced by the myelin sheath of Schwann cells.[15,16] Moreover, Aptel et al. conducted a clinical study by applying *ex vivo* THG microscopy to intact human ocular nerves to visualize myelinated nerve fibers in the subbasal layer of the cornea.[17] Several manual or automated analysis software programs have been developed for tracking continuous signals of corneal nerves with either curvilinear or linear morphological features in CCM images.[18,19] However, current methodologies have limitations for imaging the discontinuous structure of free intraepidermal nerve endings (FINEs) in human skin. No studies have demonstrated the use of THG microscopy or other imaging modalities for achieving clinical label-free imaging of discontinuous unmyelinated FINEs *in vivo*.

Small sensory nerve fibers comprise thinly myelinated Aδ fibers, which transmit sensations of cold and intense pain, and unmyelinated C fibers, which transmit sensations of warmth, heat, itch, and gradual pain, in the human skin.[20,21] FINEs, also referred to as sensory nerve terminals or nociceptors, are localized in the most superficial layer of the skin.[22] Pathological studies of FINEs in the distal part of the lower leg (10 cm above the external malleolus) are routinely performed through a technique that involves a skin biopsy followed by immunohistochemical (IHC) staining using various neuronal proteins, particularly protein gene product 9.5 (PGP9.5).[23,24] This technique is currently recommended by the European Federation of Neurological Societies for visualizing the number and morphology of FINEs.[25–28] Moreover, the density of intraepidermal nerve fibers (IENFs) can be quantitatively analyzed to distinguish patients with small-fiber neuropathy (SFN) from individuals without this condition. Morphologically, unmyelinated FINEs have a discontinuous structure and are often described as having a bead-like or pearl-like appearance in the epidermis.[29] Studies applying electron micrography have revealed that the axon diameter of unmyelinated FINEs is not fixed, but ranges from 0.2 to 1.5 μm.[30–32] In addition, studies have reported that a sudden increase in axon diameter is engendered by synapses rich in mitochondrial vesicles, glycogen granules, and other organelles, resulting in the characteristic varicose appearance.[33–35]

Here, we present an imaging methodology that focuses to detect the three-dimensional (3D) discontinuities in THG signals to provide contrast. Our study indicated that the discontinuity THG microscopy (dTHGM) can effectively identify varicose FINEs from complex signal backgrounds without requiring labeling. Moreover, we demonstrated that dTHGM can reveal varicose nerve endings under 1,260-nm femtosecond excitation. We also developed a 3D discontinuous dot-connecting algorithm for *in vivo* label-free clinical imaging of FINE structures. We conducted an examination using the nerve fiber staining agent PGP9.5, and the results confirmed that *ex vivo* dTHGM could enable label-free contrast imaging and capture the bead-like characteristics of unmyelinated human nerve fibers in the epidermis of the lower distal extremities. In addition, *in vivo* dTHGM imaging of the toe tips of mice confirmed the 3D imaging capability of our system and longitudinal assessment of a small animal model of spared nerve injury (SNI) further verified that the dTHGM signal originated from unmyelinated FINEs. Furthermore, we developed an IENF index to enable quantitative structural imaging of unmyelinated FINEs in the skin of the lower distal extremities. Our preliminary clinical assessment verified that the IENF index derived from *in vivo* dTHGM imaging could differentiate between patients with diabetic peripheral neuropathy (DPN) and controls and that the *in vivo* IENF index was highly correlated with IENF density in skin biopsies. Accordingly, our presented methodology and system can meet the clinical need for a label-free, noninvasive, and quantitative imaging tool for FINEs, which can improve screening for and differential diagnosis of DPN, surgical evaluations, and efficacy assessment of radiculopathy treatment and therapeutic strategies.

## RESULTS

### Design and principle of dTHGM for label-free imaging of discontinuous FINE bulges

Neurites, unlike regular nerve fibers in the human brain or cornea, exhibit periodic varicosities, especially in the case of FINEs in human skin. According to the literature, varicose bulges can be as large as 1.5 μm in diameter, far larger than the typically 200-nm-thick IENF.[30–32] An *ex vivo* assessment involving IHC staining with PGP9.5, as described in the following subsection, revealed that the average distance d between neighboring bulges ranges between 2.87 and 6.12 μm. The bead-string nerve structure protrudes through the epidermis and can be randomly oriented, including the vertical and horizontal directions, with respect

**Figure 1. Discontinuity THGM imaging of bead-string FINEs**

(A) Both bead-string FINEs and regular fibers oriented horizontally relative to the direction of light illumination can be visualized with a tightly focused Gaussian beam through THG. The THG signal generated by the 800-nm diameter bead is 50 times stronger than that generated by the 200-nm diameter fiber.

(B) The discontinuous varicosities of FINEs disrupt the structural axial symmetry and create the optical inhomogeneity necessary for THG generation. However, the Guoy phase shift effect can cause coherent cancellation of the THG signal due to axial symmetry if a regular fiber with a uniform diameter is stretched in the direction of light propagation. For this vertical geometry, the THG signal generated by the 800-nm diameter bead is 1 million times stronger than that generated by the 200-nm diameter fiber.

(C) The digital reconstruction of the discontinuous THG bulges within a distance of 10.4 μm can reveal FINEs.

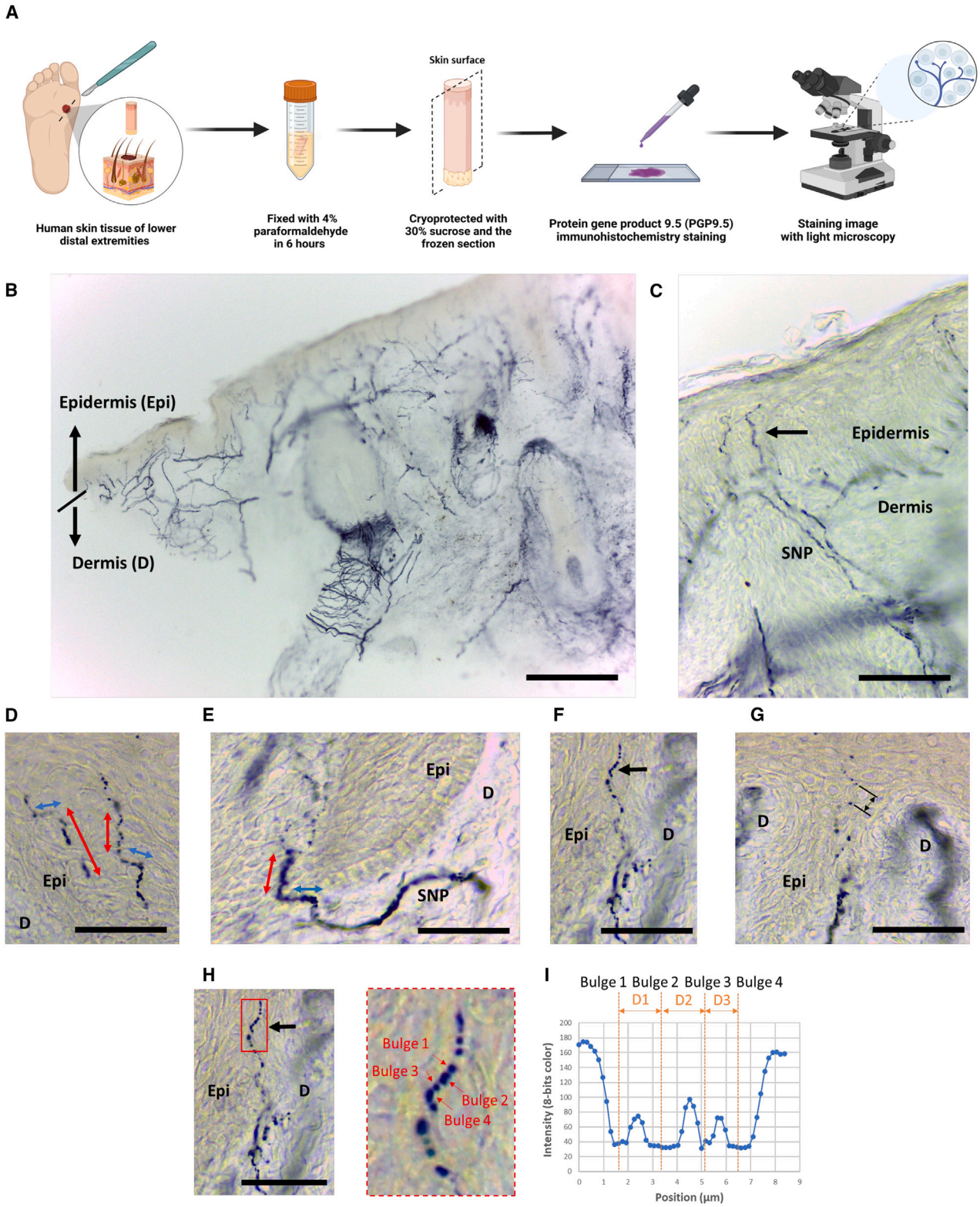


**Figure 2. Skin innervation of the sole of lower distal extremities**

(A) Immunostaining of human sole skin tissue with PGP9.5.

(B) PGP9.5 (+) nerves are in the epidermis (Epi) and in the dermis (D).

*(legend continued on next page)*

to the skin surface (Figure 1). THG, using a tightly focused Gaussian beam,[36,37] can be highly sensitive to discontinuous 3D structures owing to the Gouy phase shift effect. With a negative phase mismatch ($\Delta k < 0$), such as in skin tissue, THG is ineffective in the tightly focusing limit for any uniform structure with a length in the light illumination direction that is longer than the confocal parameter of the focused Gaussian beam.[36] This effect produces greatly different imaging results for horizontal and vertical fibers and is thus not ideal for imaging continuous uniform fiber structures, especially those that are elongated in the light illumination direction. By contrast, if the confocal parameter of the focused Gaussian beam can be designed to be on the order of or smaller than the distance d, the varicose structure can act as a spatial discontinuity to break the Guoy phase shift effect and to produce effective THG signals. By scanning a tightly focused Gaussian beam in 3D space, one can locate varicose bulges by using label-free THG signals (Figure 1A and 1B). Subsequently, digital reconstruction of the discontinuous THG bulges within a distance of 10.4 μm can reveal FINEs (Figure 1C). To image FINEs in human skin, we selected a 1,260-nm femtosecond light as our illumination source; thus, the THG wavelength was in the visible range (420 nm) to ensure high backscattering and low absorption in skin tissues. To obtain a small confocal parameter 2b, we used a high-numerical aperture (NA) objective (NA = 1.15); thus, we achieved a tight focusing effect and obtained a 2b value of 2.3 μm, on the order of the distance d with a 1.43 refractive index of skin.

### PGP9.5 immunoreactivity and varicose appearance of FINEs in human skin tissue

We conducted an immunostaining study on human sole skin tissue (Figure 2A). The tissue was determined to be richly innervated by nerve fibers that are immunoreactive with PGP9.5 (Figure 2B). PGP 9.5, a ubiquitin carboxy C-terminal hydrolase, is particularly rich in small-diameter nerves and thus has a higher total volume in enlarged bulges than in their surroundings. We observed that FINEs immunoreactive with PGP9.5 penetrated the basement membrane after arising from the subepidermal nerve plexuses and had a typical varicose appearance (Figure 2C). The unmyelinated FINEs elongated into the epidermis with multiple orientations, and the morphology of FINEs was a discontinuous bead-like pattern comprising dense varicosities (Figures 2D and 2E). Moreover, the internal distance of each varicose varied. According to our staining results, the average internal distance was 4.53 μm, which was between 1.28 and 10.4 μm (Figures 2F–2I), and it was mostly greater than the confocal parameter (theoretically ~2.3 μm) of our dTHGM system.

### *Ex vivo* tightly focused epi-THG microscopy of human skin tissue

For each unstained human skin section from the sole of the foot, 3D stacks of *ex vivo* THG images were obtained. These comprised two-dimensional (2D) *en face* images captured at various imaging depths at the dermal-epidermal junction (DEJ) (Figures 3E–3M). This imaging method is called tightly focused epi-THG microscopy (TFETM). Under the tightly focused beam with a high-NA objective lens, the label-free epi-THG signal showed representative dot-like or bead-like patterns (Figure 3L). Structures with a discontinuous bead-string appearance exhibited greater THG intensity and imaging contrast, which produced closely packed dot-like signals in the epidermis. The epi-second harmonic generation (SHG) signal was generated specifically by collagen fibers in the dermis.[38,39] This signal facilitated the task of identifying the DEJ in the human skin section. Figure 3N presents the 2D overlapped image from Figures 3E–3M; the epi-THG signals ascended perpendicularly from the dermis to the epidermis and had branches in the DEJ. In the 3D reconstructed image, the THG signal with a discontinuous bead-string pattern terminated in the upper portion of the granular layer of the skin (Figures 3O–3Q). We defined the optical propagation direction of the laser source as the z axis. TFETM enabled visualizing the dot-like or discontinuous bead-string-like epi-THG signals oriented not only vertically but also parallel to the optical axis (Figures 3R–3T). Therefore, the TFETM revealed the discontinuous characteristics of FINEs and indicated that the discontinuity THG contrast for FINE varicosity is independent of the nerve fiber orientation relative to the optical axis. To confirm the origin of the dot-like and bead-like THG signals, denoted dTHG signals, IHC staining with PGP9.5 was performed for histological validation, as described in the following section.

### *Ex vivo* histological validation of human skin sections

Immediately after the *ex vivo* TFETM imaging, human skin sections were subjected to postfixation IHC staining with PGP9.5 (Figure 4A). Figure 4 presents representative results of the histological validation studies performed on human sole skin tissues collected from three individuals. Figures 4B–4G show the corresponding 2D morphologies and positions of unmyelinated FINEs acquired through label-free TFETM imaging and through PGP9.5 IHC staining of the same human skin sections, respectively. Figures 4H and 4J present representative magnified images. The IHC staining results revealed an increase in the amount of PGP9.5 molecules in the FINE structures, as indicated by a strong blue color. Both the label-free TFETM dot-like signals and FINE structures in the stained IHC images exhibited highly consistent locations and appearances, supporting the FINE origin of the dTHG signals and also revealing the strong dTHG contrast for the varicosity structures of unmyelinated FINEs (Figures 4I and 4K). Despite not being background free, the strong dTHG contrast on the varicosity structures of unmyelinated FINEs can provide a high-contrast label-free imaging modality for capturing the morphological information of

(C) Typical epidermal nerves arise from the subepidermal nerve plexus and have a varicose appearance (arrow).
(D and E) Discontinuous FINEs are the dot-like or bead-like patterns in the epidermis with multiple extension orientations (red and blue arrows indicate vertical and horizontal orientations to the skin surface, respectively).
(F–H) The center-to-center distance between the nearest neighboring varicose bulges was 1.28–10.4 μm. (H) Magnified image of (F).
(I) The internal distance between 2 varicose bulges signals are 1.61, 1.71, and 1.28 μm for dots D1–D3, respectively.
Scale bars, 1 mm (B) and 50 μm (C–H).

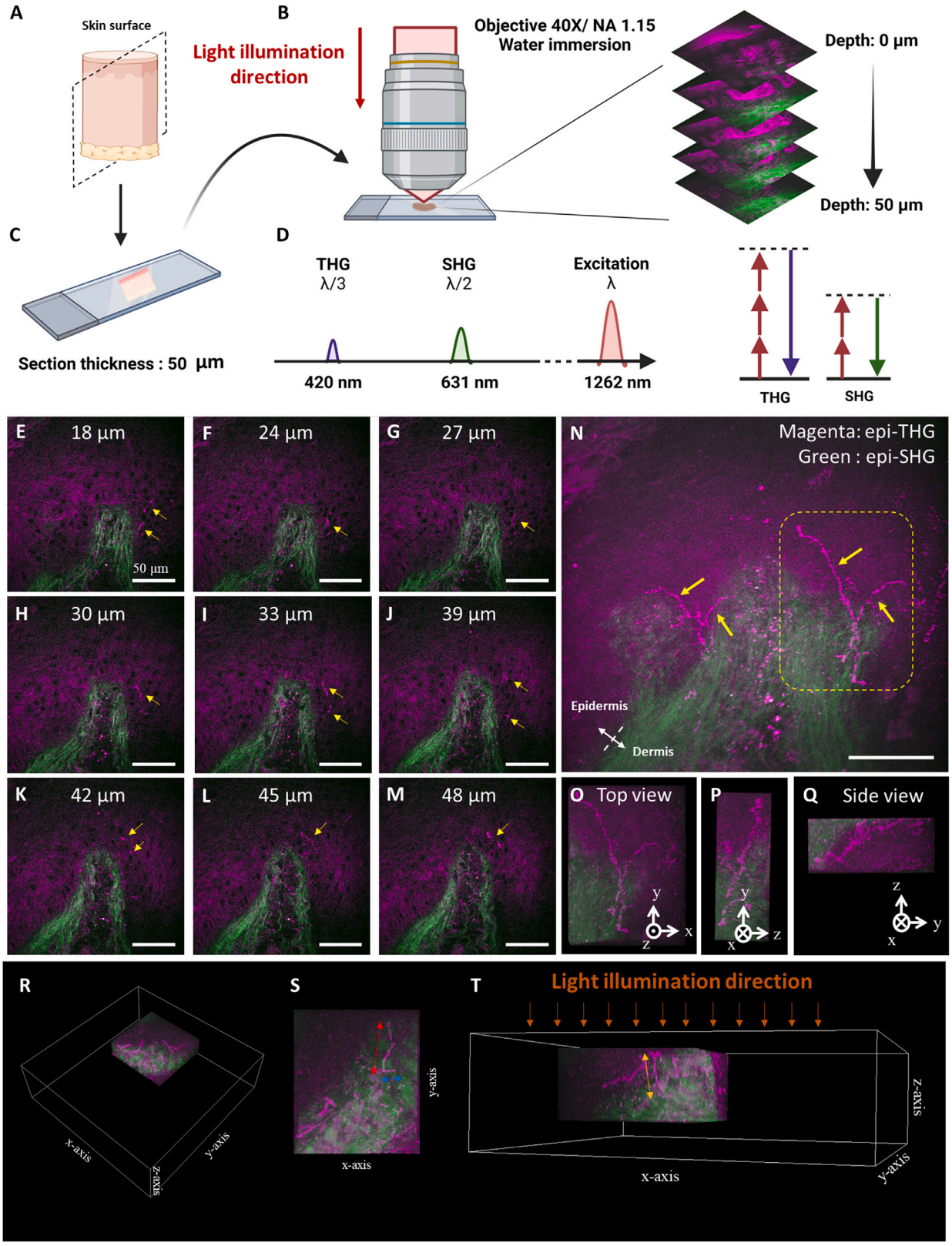


*(legend on next page)*

unmyelinated FINEs in the human epidermis with histological details. We next performed dTHGM imaging with a focus on retrieving *in vivo* dTHG signals.

### *In vivo* dTHGM observation of nerve degeneration in wild-type mice following SNI

To further confirm the capability of *in vivo* dTHGM imaging for visualizing FINEs, we used it to observe the well-known process of FINE damage in mouse toe tips in an animal model (wild-type mice: C57BL/6J Narl mice) of partial SNI (Figures 5B and 5C). For three SNI mice, we performed *in vivo* dTHGM imaging at a fixed acquisition position, which was the third toe tip of each mouse (Figure 5D), at baseline and 24 and 48 h after SNI surgery (Figure 5A). At baseline, dTHG signals with similar morphology to FINEs identified in the *ex vivo* experiment were observed at the epidermis (Figure 5E) in all three mice (Figures 5F, 5I, and 5L). Within 24 h of SNI surgery, these dTHG signals, resembling FINE varicosities, could still be observed in the epidermis of the toe tips (Figures 5G, 5J, and 5M). As expected, nerve innervation typically caused all of these epidermal dTHG signals to disappear after 48 h (Figures 5H, 5K, and 5N). These findings not only verify the capability of dTHGM for *in vivo* 3D imaging of FINEs but also demonstrate the high dTHGM contrast for FINE varicosities, which are visible as dTHG signals.

### *In vivo* dTHGM imaging in human distal skin and IENF index

Epidermal skin in the lower distal extremities is the primary target of clinical *in vivo* dTHGM imaging. After assessing various skin areas, we selected the skin of the instep arch because of its low melanin content in the basal layer and its shallower epidermal thickness (see the STAR Methods for more details). Images of unmyelinated FINEs with dot-like or bead-like structures in both the horizontal (Figures 6A–6D) and vertical directions (Figures 6E and 6F) were successfully acquired through *in vivo* dTHGM. Moreover, dTHGM revealed dot-like structures oriented in both the horizontal and vertical directions in all of the samples used in *ex vivo* and *in vivo* human and animal studies; hence, we conclude that dTHGM is sensitive to the varicose structure in FINEs. Based on this conclusion and our PGP9.5 IHC staining data, we developed an IENF index based on a discontinuous dot-connecting algorithm for quantitatively analyzing and identifying FINE signals (Figure 7; see the STAR Methods for more details). We analyzed our *in vivo* clinical study results by comparing IENF index values between a DPN group (n = 3) and a control group (n = 11). The IENF index of the DPN group (mean ± SD, 19.7 ± 11.97 fibers/mm$^2$) was significantly lower than that of the control group (36.79 ± 7.79 fibers/mm$^2$; p = 0.0102, standard t test), as shown in Figure 6G. Moreover, the IENF index was significantly correlated with the IENF density of skin biopsies for the three patients with DPN (Pearson's correlation coefficient $R$ = 0.982; $R^2$ = 0.964; Figure 6H).

## DISCUSSION

PN is the most common type of neuropathy, affecting hundreds of millions of people.[40] SFN is a subtype of PN affecting the thinly myelinated Aδ or the nonmyelinated C fibers, constituting 79.6%–91.4% of peripheral nerve fibers.[41,42] Diabetes and prediabetes frequently are associated with SFN.[43] Diagnosing SFN is currently challenging because physical examinations and painful NCSs primarily detect large sensory nerves; they are ineffective for the functional assessment of small sensory nerves.[44] Quantitative sensory testing (QST) has been commonly used for functional assessments of sensory nerve fibers in patients with SFN; however, it is psychophysically subjective and highly dependent on the experience of the assessor and the testing environment.[45–47] Therefore, QST is more suitable for studying changes in populations over time than as a diagnostic tool for individual patients.[48] Although the skin biopsy may not offer a definitive diagnosis, it provides valuable IENF density information.[23–28] IENF density assessment has been known to be one of the most sensitive diagnostic methods for length-dependent SFN[23–28] and could provide helpful information in the evaluation of diabetic neuropathy.[23,26,49] Nevertheless, invasive skin biopsies, which can cause skin wounds,[50] are particularly dangerous for patients with diabetic coagulation abnormalities. Moreover, IHC staining is difficult to standardize, resulting in variability between laboratories.[51] Thus, label-free, slide-free, and noninvasive imaging techniques for observing FINEs with native contrast are essential for reducing harm to patients and potential medical risks.

Here, we present a dTHGM methodology—along with its mechanism and design—that is tailored to reveal the clinical bead-string features of unmyelinated FINEs. To confirm that dTHGM can achieve label-free FINE imaging, we conducted an *ex vivo* study to compare its performance with that of IHC staining with PGP9.5 (the gold standard). Our comparison confirmed that the contrast of the dTHG signals could reveal the bulges of the free nerve endings. A longitudinal in an SNI animal model revealed bead-string-like label-free dTHG signals *in vivo* at baseline, which disappeared completely 48 h after nerve injury. This phenomenon is consistent with the findings of previous studies,[52,53] which have

**Figure 3. *Ex vivo* TFETM imaging of human skin tissue from the sole of lower distal extremities**

(A) The human sole skin tissue was sectioned longitudinally. The dashed plane is the frozen section plane.

(B) To achieve a tightly focused laser beam, a 1.15-NA objective was used to focus the laser beam onto the skin section.

(C) The thickness of each skin section was 50 μm.

(D) Spectral representation (left) of the signals created by excitation at λ = 1,262 nm. THG and SHG signals are generated at one-third and one-half, respectively, of the excitation wavelength. Right, corresponding simplified Jablonski diagrams; dashed lines, virtual states.

(E–M) 2D *en face* images with different imaging depths at the DEJ and the dot-like or bead-like dTHG signals (yellow arrows) in the epidermis.

(N) 2D overlapped image produced from (E)–(M). Label-free epi-THG signals ascended perpendicularly from the dermis to the epidermis and had branches in the DEJ.

(O–Q) 3D reconstruction images showing the label-free dTHG signals in the epidermis.

(R–T) Epi-THG signals oriented perpendicular (red and blue) or parallel (yellow) to the optical z axis were observed.

Scale bars, 50 μm.

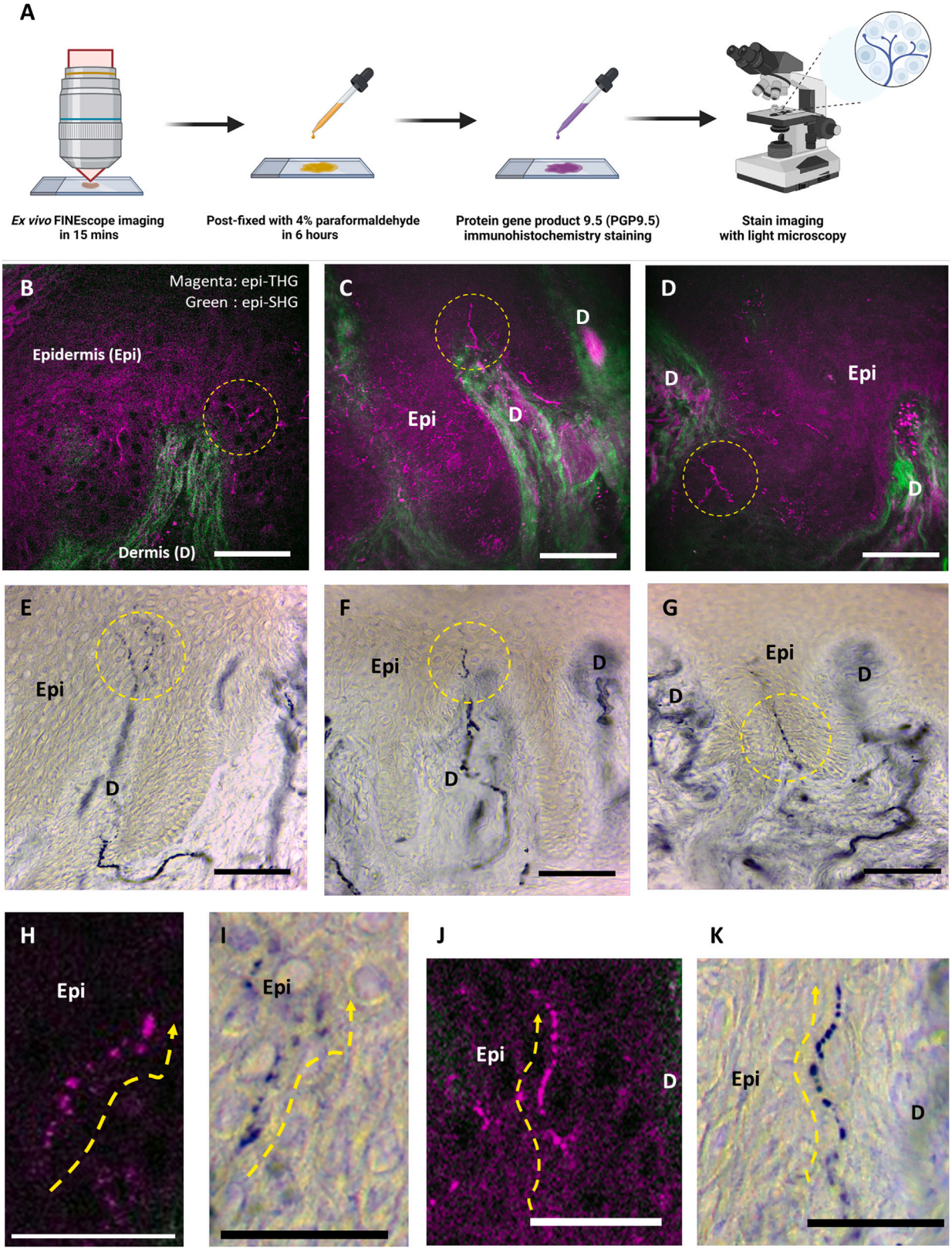


*(legend on next page)*

reported the degeneration of FINEs 48 h after nerve injury, thus further confirming that the dTHG signals can reveal *in vivo* discontinuities of unmyelinated FINEs. Our *in vivo* preliminary clinical study demonstrated that *in vivo* dTHGM with a tightly focused near-infrared laser beam could enable label-free imaging of unmyelinated FINEs. Furthermore, we derived an IENF index on the basis of a dot-connecting protocol to analyze the *in vivo* label-free dTHGM results. This index could be used to noninvasively differentiate between DPN and control groups. Moreover, the IENF index was highly correlated with the IENF density of skin biopsies in the DPN group. The epi-SHG modality, with connective tissue contrast[38,39] that is typical of the dermis, can assist in identifying the DEJ. Our findings support that the discontinuous dot-connecting THGM can be used as a noninvasive, label-free, quantitative, and objective tool for FINE imaging and the differential diagnosis of DPN. Our system has excellent potential for use in screening and assessment applications for radiculopathy treatment.

### CCM in neuropathic patients

CCM has emerged as an *in vivo* ophthalmic imaging modality for evaluating small nerve fiber morphometry in Bowman's layer, which is located below the basal layer in the cornea.[54,55] Several studies have reported that CCM can detect damaged nerve fibers in neuropathic patients[56,57] and has comparable diagnostic efficiency to skin biopsies.[58] However, CCM provides contrast for only myelinated axons. Furthermore, Ziegler et al. reported that although CCM and skin biopsies can both detect nerve fiber loss in patients with recently diagnosed type 2 diabetes, they are typically only effective in different patients, suggesting a low correlation between CCM and skin biopsy-derived IENF density.[59] These results suggest that SFN does not develop simultaneously in different organs; thus, nerve fiber damage in the cornea does not directly reflect that in the skin of the distal extremities. However, DPN is typically chronic, in which nerve fiber damage starts from the distal limbs and then spreads to the proximal limbs, suggesting that DPN first develops in the skin of the distal extremities. Our findings suggest that dTHGM is more suitable than CCM for noninvasive label-free imaging of FINEs in human skin, especially in the lower distal extremities, for the differential diagnosis of DPN.

### Other noninvasive optical imaging techniques

Optical coherence tomography (OCT) can be used to obtain histopathological skin images with a high penetration capability. However, because OCT has poor spatial resolution, it cannot acquire neural information for FINEs on a submicrometer scale.[60,61] Myelin can produce photoacoustic signals; hence, photoacoustic microscopy (PAM) can visualize myelinated mouse sciatic nerves *ex vivo*.[62] Reflection confocal microscopy (RCM) can provide information on myelinated nerves in the deep brain regions of mice[63] or transgenic zebrafish[64] with strong contrast due to the high refractive index of lipid-rich myelin. Although PAM and RCM provide high-resolution images in the human skin and seem to be attractive choices for such imaging, no studies have reported that they can image unmyelinated nerve fibers, especially the distal nerve endings of C fibers.

In summary, FINEs are the most abundant sensing organs for detecting temperature, touch, and painful stimuli. Currently, pathological diagnosis based on surgically excised tissue followed by formalin-fixed and histochemical staining is the gold standard in clinical practice. Despite removing the affected skin and nerve, these methods cannot achieve longitudinal observations of the targeted FINEs. Here, we propose and demonstrate a label-free imaging modality, dTHGM, and confirm that it can reveal the bead-string-like nature of FINEs, thus serving as an ideal noninvasive skin biopsy method for unmyelinated FINE imaging. Specifically, dTHGM could reveal the 3D structure of unmyelinated FINEs, and its results were confirmed by PGP9.5 IHC staining of the same tissue section. We further developed a discontinuous dot-connecting algorithm to determine the IENF index in a fixed area, which we noted to be nearly perfectly correlated with the quantitative IENF density. Thus, dTHGM is a paradigm-shifting imaging technique for quantitatively determining the IENF density, potentially replacing traditional skin biopsy methods. Moreover, this real-time, repeatable, noninvasive imaging system could serve as a powerful method for the longitudinal monitoring of FINE regeneration and degeneration throughout the clinical course of diabetic, chemotherapy-induced, or postherpetic neuropathy.

### Limitations of the study

The study is subject to several limitations. First, the sample size of patients with DPN could be increased to enhance the reliability and generalizability of the findings. Second, a broader range of ages and genders should be included in the control group to ensure a more comprehensive comparison. Third, an independent study that excludes the influence of diabetes is necessary to discern whether observed effects are specific to DPN or generalizable to neuropathy in other contexts. Lastly, conducting skin biopsies in the control group would provide valuable baseline data for comparison, potentially yielding deeper insights into the characteristics of IENFs.

## STAR★METHODS

Detailed methods are provided in the online version of this paper and include the following:

**Figure 4. Representative results of histological validation studies performed on human skin tissue from the lower distal extremities**

(A) Process of postfixation IHC staining of the human sole skin sections with PGP9.5. Staining was conducted immediately after the *ex vivo* TFETM imaging.

(B–D) Label-free epi-THG signals (yellow circles) in the epidermis of the skin sections for unmyelinated FINEs.

(E and F) Corresponding FINEs with similar morphology and position to those in (B)–(D) acquired using immunolabeling imaging with PGP9.5 IHC from the same human skin sections.

(H and J) Label-free epi-THG signal with a bead-string-like discontinuous structure (yellow dashed lines with arrows); these dTHG signals were confirmed to represent the varicose structure of unmyelinated FINEs through PGP9.5 IHC staining, as shown in (I) and (K).

Scale bars, 50 μm. Epi: epidermis; D: dermis.

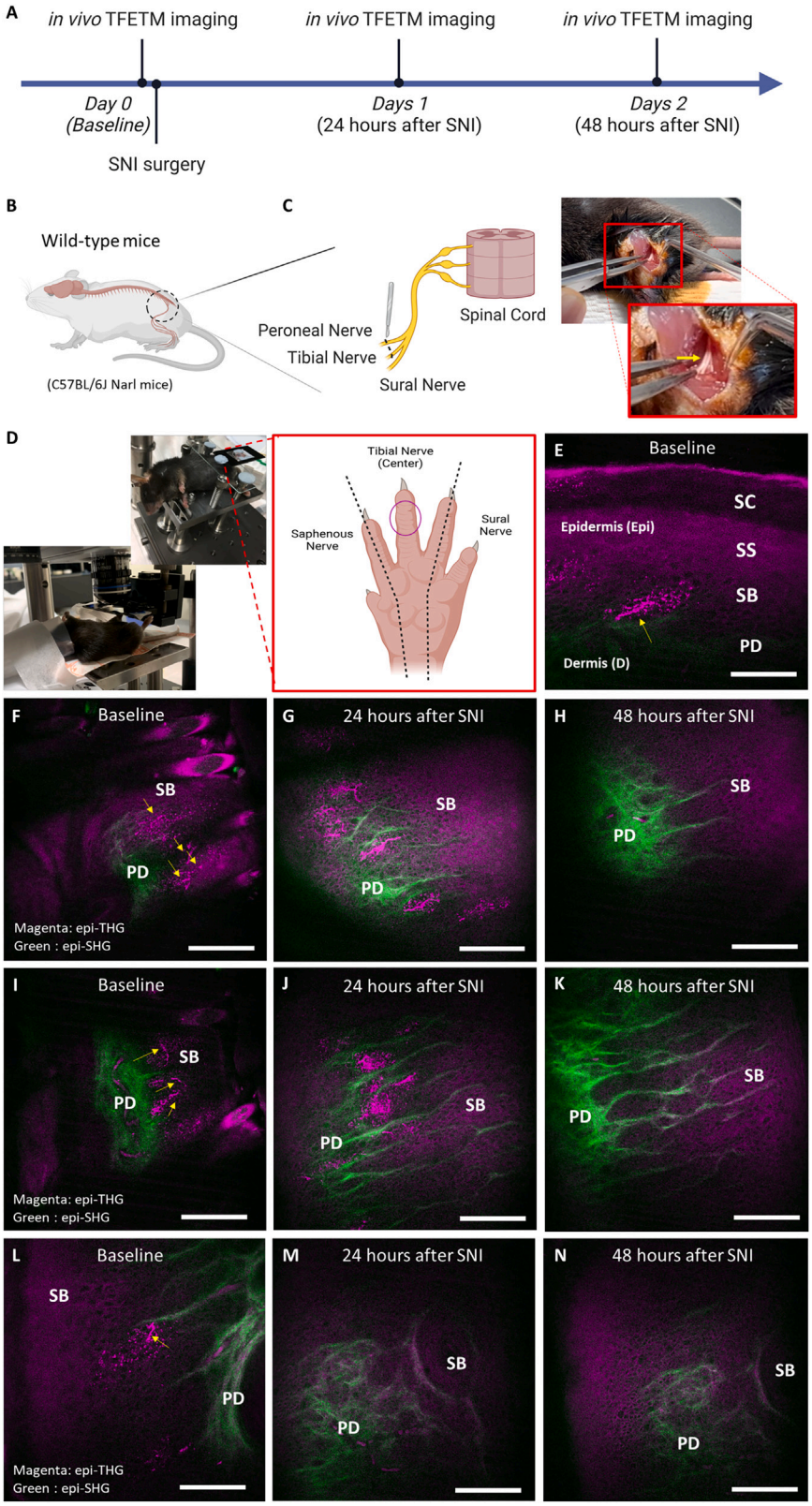


**Figure 5. Longitudinal observation of nerve innervation and degeneration in mouse toe tips before and after SNI surgery with *in vivo* dTHGM imaging**

(A) *In vivo* dTHGM imaging at a fixed acquisition position was performed before SNI surgery (baseline) and 24 and 48 h after SNI surgery.

(B) Location of SNI surgery on wild-type mouse (C57BL/6J Narl mice) for observing damage to FINEs in the mouse toe tips.

(C) In the SNI surgery, the tibial nerve and common peroneal nerve were ligated and cut (yellow arrow).

(D) SNI surgery led to complete denervation of the tibial (central) innervated area of the hind paw glabrous skin. The acquisition position for *in vivo* dTHGM imaging was at the third toe tip (purple circle).

(E) Before SNI surgery, the nerve fibers could be observed with TFETM signals (yellow arrow) ascending from the papillary dermis (PD) to the stratum spinosum (SS) layers in the epidermis.

(F, I, and L) For all 3 mice, the FINEs had a dTHG pattern (yellow arrow) in the epidermis of the third mouse toe tip at baseline.

(G, H, J, M, and N) After SNI surgery, the FINEs with dTHG signals started to degenerate and completely disappeared after 24 h (G, J, and M) and 48 h (H, J, and N).

Scale bars, 50 μm. SB, stratum basale; SC, stratum corneum.

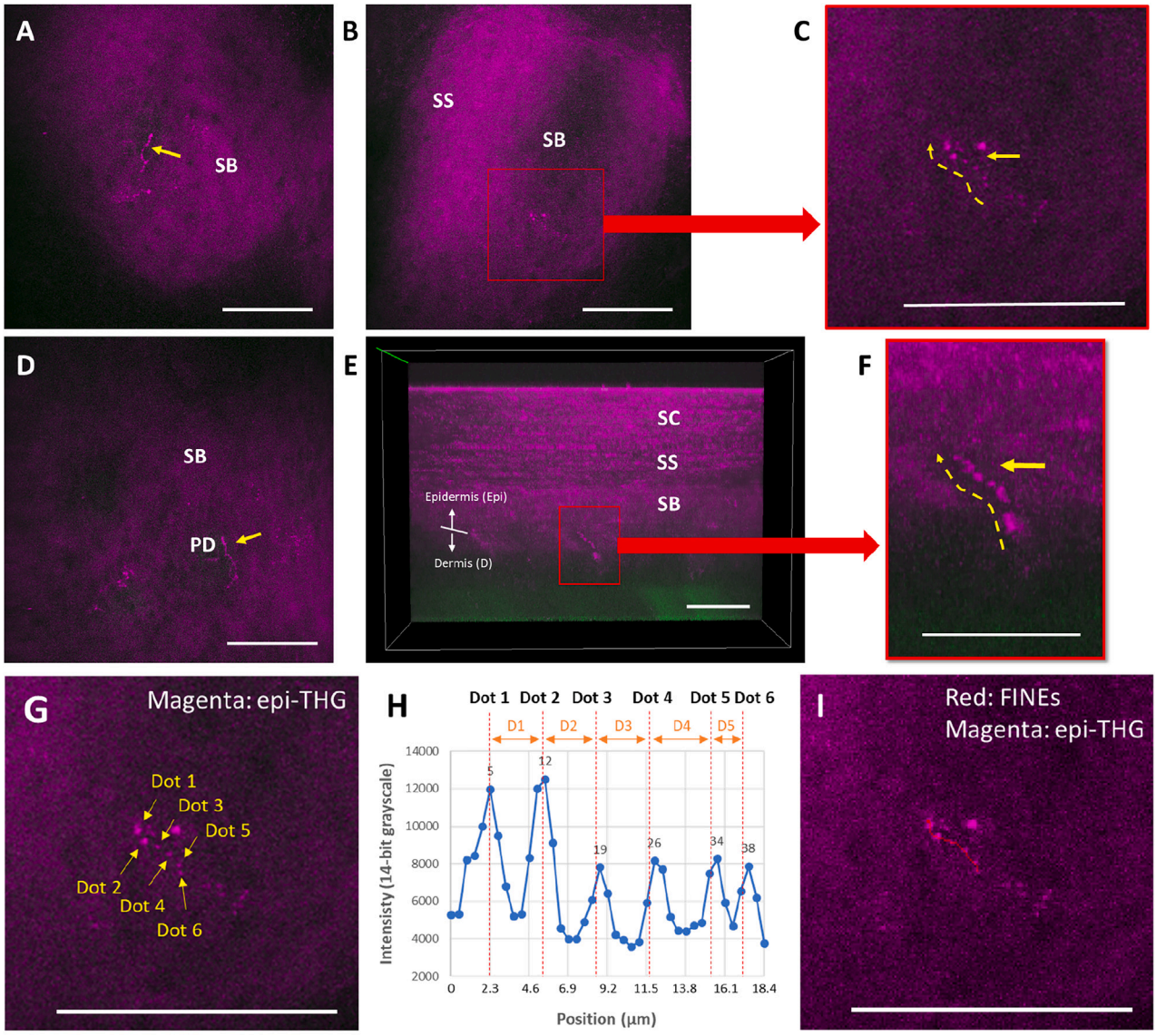


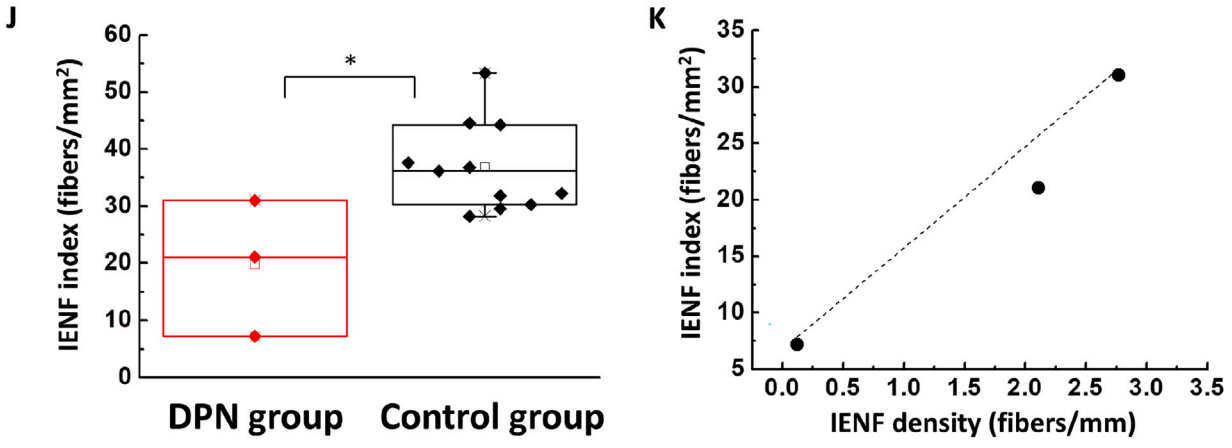


(legend on next page)

## ACKNOWLEDGMENTS

We are indebted to the patients who participated in the clinical trials. This work was sponsored by the National Science and Technology Council, Taiwan, under MOST 107-2321-B-002-006, MOST 110-2221-E-002-048-MY3, and NSTC 112-2321-B-002-019, and the Ministry of Economic Affairs under 111-EC-17-A-19-S6-009.

## AUTHOR CONTRIBUTIONS

C.-K.S., P.-J.W., S.-T.H, W.-Z.S., and C.-T.Y designed the experiment. P.-J.W and H.-C.T. built the microscopy system, performed the experiments, and analyzed the data. C.-K.S. supervised the project. C.-T.Y. and W.-Y.L. assisted in the small animal experiment. S.-T.H., C.-C.C., and Y.-H.L. recruited the volunteers. W.-Z.S., S.-T.H., C.-C.C., and Y.-H.L. conducted the clinical trial. S.-T.H. and C.-C.C. performed the skin biopsy. All of the authors were involved in discussions during the work and in the preparation of the manuscript.

## DECLARATION OF INTERESTS

The disclosed protocol is under patent applications entitled "A METHOD AND APPARATUS FOR NON-INVASIVE IMAGE-OBSERVING DENSITY OF INTRAEPIDERMAL NERVE FIBER OF HUMAN SKIN."

Received: August 14, 2023
Revised: January 4, 2024
Accepted: February 26, 2024
Published: March 18, 2024

## REFERENCES

1. Harel, N.Y., and Strittmatter, S.M. (2008). Functional MRI and other non-invasive imaging technologies: providing visual biomarkers for spinal cord structure and function after injury. Exp. Neurol. *211*, 324–328. https://doi.org/10.1016/j.expneurol.2008.02.017.
2. Rangavajla, G., Mokarram, N., Masoodzadehgan, N., Pai, S.B., and Bellamkonda, R.V. (2014). Noninvasive imaging of peripheral nerves. Cells Tissues Organs *200*, 69–77. https://doi.org/10.1159/000369451.
3. Fornito, A., Zalesky, A., and Bullmore, E. (2016). Fundamentals of Brain Network Analysis (Academic Press).
4. Hagmann, P., Kurant, M., Gigandet, X., Thiran, P., Wedeen, V.J., Meuli, R., and Thiran, J.P. (2007). Mapping human whole-brain structural networks with diffusion MRI. PLoS One *2*, e597. https://doi.org/10.1371/journal.pone.0000597.
5. Romano, N., Federici, M., and Castaldi, A. (2019). Imaging of cranial nerves: a pictorial overview. Insights Imaging *10*, 33. https://doi.org/10.1186/s13244-019-0719-5.
6. Roberts, T.P.L., and Mikulis, D. (2007). Neuro MR: principles. J. Magn. Reson. Imaging. *26*, 823–837. https://doi.org/10.1002/jmri.21029.
7. Mori, S., and Zhang, J. (2006). Principles of diffusion tensor imaging and its applications to basic neuroscience research. Neuron *51*, 527–539. https://doi.org/10.1016/j.neuron.2006.08.012.
8. Sheikh, K.A. (2010). Non-invasive imaging of nerve regeneration. Exp. Neurol. *223*, 72–76. https://doi.org/10.1016/j.expneurol.2009.07.008.
9. Zaottini, F., Picasso, R., Pistoia, F., Sanguinetti, S., Pansecchi, M., Tovt, L., Viglino, U., Cabona, C., Garnero, M., Benedetti, L., and Martinoli, C. (2022). High resolution ultrasound of peripheral neuropathies in rheumatological patients: an overview of clinical applications and imaging findings. Front. Med. *9*, 984379. https://doi.org/10.3389/fmed.2022.984379.x.
10. El Miedany, Y.M., Aty, S.A., and Ashour, S. (2004). Ultrasonography versus nerve conduction study in patients with carpal tunnel syndrome: substantive or complementary tests? Rheumatology *43*, 887–895. https://doi.org/10.1093/rheumatology/keh190.
11. Petropoulos, I.N., Manzoor, T., Morgan, P., Fadavi, H., Asghar, O., Alam, U., Ponirakis, G., Dabbah, M.A., Chen, X., Graham, J., et al. (2013). Repeatability of *in vivo* corneal confocal microscopy to quantify corneal nerve morphology. Cornea *32*, e83–e89. https://doi.org/10.1097/ICO.0b013e3182749419.
12. Débarre, D., Supatto, W., Pena, A.M., Fabre, A., Tordjmann, T., Combettes, L., Schanne-Klein, M.C., and Beaurepaire, E. (2006). Imaging lipid bodies in cells and tissues using third-harmonic generation microscopy. Nat. Methods *3*, 47–53. https://doi.org/10.1038/nmeth813.

**Figure 6. Representative *in vivo* clinical dTHGM images from the skin of the instep arch in the lower distal extremities and quantitative IENF index values derived for patients with DPN and controls**

(A and D) Label-free bead-string-like *in vivo* dTHG signals (yellow arrows) in the human epidermis.
(B and E) Typical varicose structure (red squares) appeared for the unmyelinated FINEs in the epidermis.
(C and F) Magnified images revealing the varicose structures of 1 horizontally and 1 vertically oriented unmyelinated FINE with respect to the skin surface.
(G) A representative FINE signal showing at least 5 consecutive dot-like signals.
(H) The internal distance between 2 successive dot-like THG signals should be within 10.4 μm; these are 3.2, 3.2, 3.2, 3.7, and 1.8 μm for dots D1–D5, respectively.
(I) The same *in vivo* dTHGM image as (G) after discontinuous dot connection (red line) as 1 IENF.
(J) Patients with DPN had significantly lower IENF index values than did controls (*$p < 0.05$; **$p < 0.01$).
(K) The IENF index values of patients with DPN and the IENF density derived from skin biopsies (on the distal part of the lower leg, 10 cm above the external malleolus) were highly correlated (Pearson's correlation coefficient $R = 0.98$).
Scale bars, 50 μm.

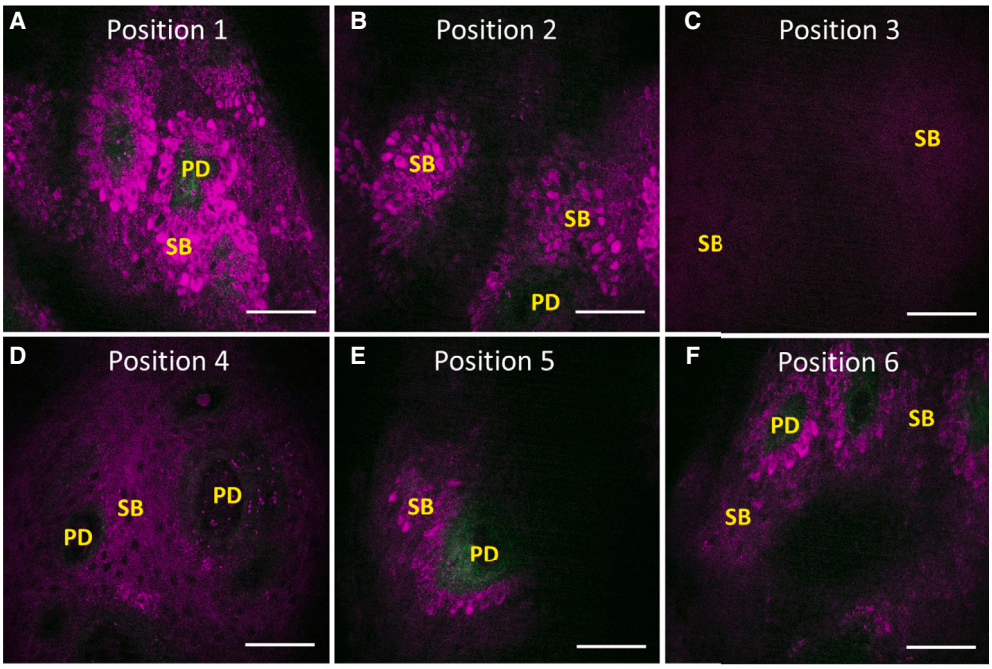


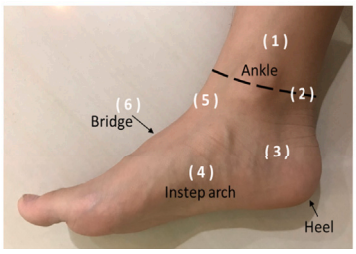


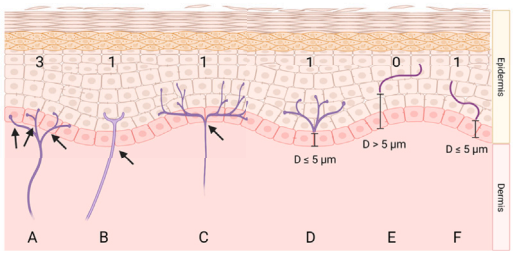


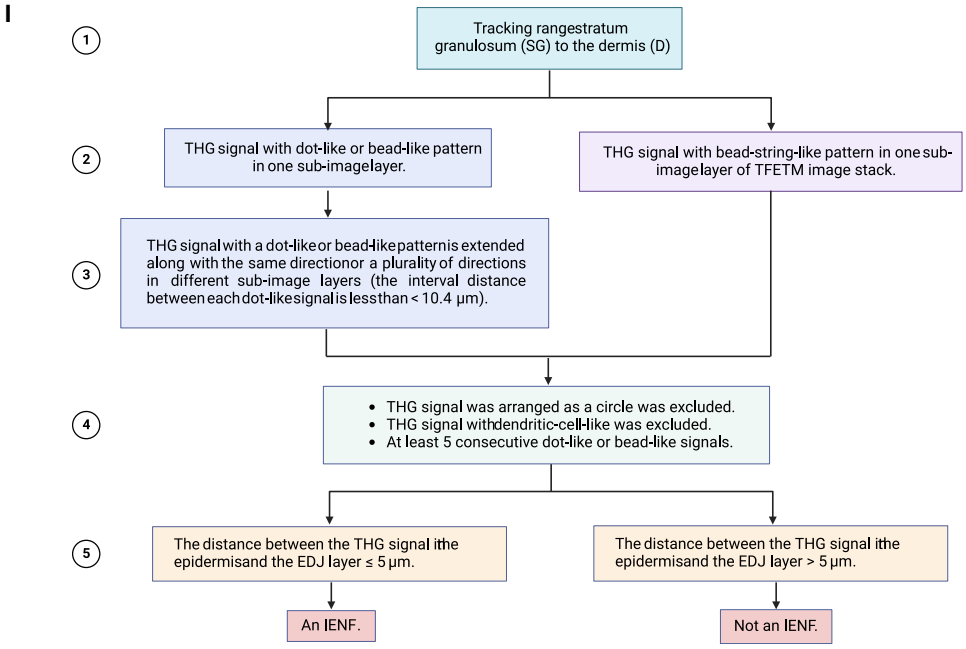


*(legend on next page)*

13. Redlich, M.J., Prall, B., Canto-Said, E., Busarov, Y., Shirinyan-Tuka, L., Meah, A., and Lim, H. (2021). High-pulse-energy multiphoton imaging of neurons and oligodendrocytes in deep murine brain with a fiber laser. Sci. Rep. *11*, 7950. https://doi.org/10.1038/s41598-021-86924-6.

14. Witte, S., Negrean, A., Lodder, J.C., de Kock, C.P.J., Testa Silva, G., Mansvelder, H.D., and Louise Groot, M. (2011). Label-free live brain imaging and targeted patching with third-harmonic generation microscopy. Proc. Natl. Acad. Sci. USA *108*, 5970–5975. https://doi.org/10.1073/pnas.1018743108.

15. Lim, H., Sharoukhov, D., Kassim, I., Zhang, Y., Salzer, J.L., and Melendez-Vasquez, C.V. (2014). Label-free imaging of Schwann cell myelination by third harmonic generation microscopy. Proc. Natl. Acad. Sci. USA *111*, 18025–18030. https://doi.org/10.1073/pnas.1417820111.

16. Hajjar, H., Boukhaddaoui, H., Rizgui, A., Sar, C., Berthelot, J., Perrin-Tricaud, C., Rigneault, H., and Tricaud, N. (2018). Label-free non-linear microscopy to measure myelin outcome in a rodent model of Charcot-Marie-Tooth diseases. J. Biophot. *11*, e201800186. https://doi.org/10.1002/jbio.201800186.

17. Aptel, F., Olivier, N., Deniset-Besseau, A., Legeais, J.M., Plamann, K., Schanne-Klein, M.C., and Beaurepaire, E. (2010). Multimodal nonlinear imaging of the human cornea. Invest. Ophthalmol. Vis. Sci. *51*, 2459–2465. https://doi.org/10.1167/iovs.09-4586.

18. Alam, U., Anson, M., Meng, Y., Preston, F., Kirthi, V., Jackson, T.L., Nderitu, P., Cuthbertson, D.J., Malik, R.A., Zheng, Y., and Petropoulos, I.N. (2022). Artificial intelligence and corneal confocal microscopy: the start of a beautiful relationship. J. Clin. Med. *11*, 6199. https://doi.org/10.3390/jcm11206199.

19. Dabbah, M.A., Graham, J., Petropoulos, I.N., Tavakoli, M., and Malik, R.A. (2011). Automatic analysis of diabetic peripheral neuropathy using multi-scale quantitative morphology of nerve fibres in corneal confocal microscopy imaging. Med. Image Anal. *15*, 738–747. https://doi.org/10.1016/j.media.2011.05.016.

20. Raasing, L.R.M., Vogels, O.J.M., Veltkamp, M., van Swol, C.F.P., and Grutters, J.C. (2021). Current view of diagnosing small fiber neuropathy. J. Neuromuscul. Dis. *8*, 185–207. https://doi.org/10.3233/JND-200490.

21. Pittenger, G.L., Ray, M., Burcus, N.I., McNulty, P., Basta, B., and Vinik, A.I. (2004). Intraepidermal nerve fibers are indicators of small-fiber neuropathy in both diabetic and nondiabetic patients. Diabetes Care *27*, 1974–1979. https://doi.org/10.2337/diacare.27.8.1974.

22. Delmas, P., Hao, J., and Rodat-Despoix, L. (2011). Molecular mechanisms of mechanotransduction in mammalian sensory neurons. Nat. Rev. Neurosci. *12*, 139–153. https://doi.org/10.1038/nrn2993.

23. Lauria, G., McArthur, J.C., Hauer, P.E., Griffin, J.W., and Cornblath, D.R. (1998). Neuropathological alterations in diabetic truncal neuropathy: evaluation by skin biopsy. J. Neurol. Neurosurg. Psychiatry *65*, 762–766. https://doi.org/10.1136/jnnp.65.5.762.

24. Kennedy, W.R., and Wendelschafer-Crabb, G. (1993). The innervation of human epidermis. J. Neurol. Sci. *115*, 184–190. https://doi.org/10.1016/0022-510x(93)90223-l.

25. Holland, N.R., Crawford, T.O., Hauer, P., Cornblath, D.R., Griffin, J.W., and McArthur, J.C. (1998). Small-fiber sensory neuropathies: clinical course and neuropathology of idiopathic cases. Ann. Neurol. *44*, 47–59. https://doi.org/10.1002/ana.410440111.

26. Kennedy, W.R., Wendelschafer-Crabb, G., and Johnson, T. (1996). Quantitation of epidermal nerves in diabetic neuropathy. Neurology *47*, 1042–1048. https://doi.org/10.1212/wnl.47.4.1042.

27. McCarthy, B.G., Hsieh, S.T., Stocks, A., Hauer, P., Macko, C., Cornblath, D.R., Griffin, J.W., and McArthur, J.C. (1995). Cutaneous innervation in sensory neuropathies: evaluation by skin biopsy. Neurology *45*, 1848–1855. https://doi.org/10.1212/wnl.45.10.1848.

28. Lauria, G., Hsieh, S.T., Johansson, O., Kennedy, W.R., Leger, J.M., Mellgren, S.I., Nolano, M., Merkies, I.S.J., Polydefkis, M., Smith, A.G., et al. (2010). European Federation of Neurological Societies/Peripheral Nerve Society Guideline on the use of skin biopsy in the diagnosis of small fiber neuropathy. Report of a joint task force of the European Federation of Neurological Societies and the Peripheral Nerve Society. Eur. J. Neurol. *17*, 903–e49, e44–e49. https://doi.org/10.1111/j.1468-1331.2010.03023.x.

29. McDougall, J.J. (2006). Arthritis and pain. Neurogenic origin of joint pain. Arthritis Res. Ther. *8*, 220. https://doi.org/10.1186/ar2069.

30. Julius, D., and Basbaum, A.I. (2001). Molecular mechanisms of nociception. Nature *413*, 203–210. https://doi.org/10.1038/35093019.

31. Oaklander, A.L., and Siegel, S.M. (2005). Cutaneous innervation: form and function. J. Am. Acad. Dermatol. *53*, 1027–1037. https://doi.org/10.1016/j.jaad.2005.08.049.

32. Mihara, M. (1984). Regenerated cutaneous nerves in human epidermal and subepidermal regions. An electron microscopy study. Arch. Dermatol. Res. *276*, 115–122. https://doi.org/10.1007/BF00511068.

33. Shepherd, G.M.G., and Raastad, M. (2003). Axonal varicosity distributions along parallel fibers: a new angle on a cerebellar circuit. Cerebellum *2*, 110–113. https://doi.org/10.1080/14734220310011407.

34. Novotny, G.E., and Gommert-Novotny, E. (1988). Intraepidermal nerves in human digital skin. Cell Tissue Res. *254*, 111–117. https://doi.org/10.1007/BF00220023.

35. Rajan, B., Polydefkis, M., Hauer, P., Griffin, J.W., and McArthur, J.C. (2003). Epidermal reinnervation after intracutaneous axotomy in man. J. Comp. Neurol. *457*, 24–36. https://doi.org/10.1002/cne.10460.

36. Boyd, R.W. (2020). Nonlinear Optics (Academic Press). Chapter 2.

37. Yelin, D., and Silberberg, Y. (1999). Laser scanning third-harmonic-generation microscopy in biology. Opt Express *5*, 169–175. https://doi.org/10.1364/oe.5.000169.

38. Chu, S.-W., Tai, S.-P., Chan, M.-C., Sun, C.-K., Hsiao, I.-C., Lin, C.-H., Chen, Y.C., and Lin, B.-L. (2007). Thickness dependence of optical second harmonic generation in collagen fibrils. Opt Express *15* (*19*), 12005–12010.

39. Chen, S.-Y., Chen, S.U., Wu, H.Y., Lee, W.J., Liao, Y.H., and Sun, C.-K. (2009). *In vivo* virtual biopsy of human skin by using noninvasive higher harmonic generation microscopy. IEEE J. Sel. Top. Quant. Electron. *16*, 478–492.

40. Hammi, C., and Yeung, B. (2022). Neuropathy (StatPearls Publishing).

**Figure 7. *In vivo* TFETM images acquired from different positions of the distal leg and a diagram of skin innervation with discontinuous-dot-connecting algorithm flowchart**

(A, B, E, and F) High melanin content in the basal layers generates a strong epi-THG background in the *in vivo* TFETM images.

(C and D) Positions 3 and 4 had much lower basal-layer melanin content; the background epi-THG signal was weaker in position 3 than in position 4.

(G) Corresponding positions for (A)–(F) on the foot. Position 1 was above the ankle, position 2 was on the ankle, position 3 was on the side of the heel, position 4 was at the instep arch, position 5 was between the ankle and the bridge, and position 6 was on the bridge.

(H) Diagram of skin innervation. FINEs are shown in magenta. (Case A) FINEs with branching points in the DEJ or dermis were counted separately. (Cases B and C) FINEs with a branching point in the epidermis was considered as 1 IENF. (Case E) Fragments further than 5 μm from the DEJ were not counted as IENFs. (Cases D and F) Fragments closer than 5 μm to the DEJ were counted as IENFs.

(I) Flowchart of the discontinuous dot-connecting algorithm.

Scale bars, 50 μm.

41. Said, G., Baudoin, D., and Toyooka, K. (2008). Sensory loss, pains, motor deficit and axonal regeneration in length-dependent diabetic polyneuropathy. J. Neurol. *255*, 1693–1702. https://doi.org/10.1007/s00415-008-0999-z.

42. Malik, R.A., Tesfaye, S., Newrick, P.G., Walker, D., Rajbhandari, S.M., Siddique, I., Sharma, A.K., Boulton, A.J.M., King, R.H.M., Thomas, P.K., and Ward, J.D. (2005). Sural nerve pathology in diabetic patients with minimal but progressive neuropathy. Diabetologia *48*, 578–585. https://doi.org/10.1007/s00125-004-1663-5.

43. Hovaguimian, A., and Gibbons, C.H. (2011). Diagnosis and Treatment of Pain in Small Fiber Neuropathy. Curr. Pain Headache Rep. *15*, 193–200.

44. Hoeijmakers, J.G., Faber, C.G., Lauria, G., Merkies, I.S., and Waxman, S.G. (2012). Small-fibre neuropathies–advances in diagnosis, pathophysiology and management. Nat. Rev. Neurol. *8*, 369–379. https://doi.org/10.1038/nrneurol.2012.97.

45. Hansson, P., Backonja, M., and Bouhassira, D. (2007). Usefulness and limitations of quantitative sensory testing: clinical and research application in neuropathic pain states. Pain *129*, 256–259. https://doi.org/10.1016/j.pain.2007.03.030.

46. Dyck, P.J., Dyck, P.J., Kennedy, W.R., Kesserwani, H., Melanson, M., Ochoa, J., Shy, M., Stevens, J.C., Suarez, G.A., and O'Brien, P.C. (1998). Limitations of quantitative sensory testing when patients are biased toward a bad outcome. Neurology *50*, 1213. https://doi.org/10.1212/wnl.50.5.1213.

47. Freeman, R., Chase, K.P., and Risk, M.R. (2003). Quantitative sensory testing cannot differentiate simulated sensory loss from sensory neuropathy. Neurology *60*, 465–470. https://doi.org/10.1212/wnl.60.3.465.

48. Lauria, G., Merkies, I.S.J., and Faber, C.G. (2012). Small fibre neuropathy. Curr. Opin. Neurol. *25*, 542–549. https://doi.org/10.1097/WCO.0b013e32835804c5.

49. Sarah, T., Jonathan, E., Andrew, K., Luke, R., Lana, H., Will, H., Andrea, C., and Douglas, W. (2023). Abnormal intraepidermal nerve fiber density in disease: A scoping review. Front. Neurol. *14*, 1161077.

50. Abhishek, K., and Khunger, N. (2015). Complications of skin biopsy. J. Cutan. Aesthetic Surg. *8*, 239–241. https://doi.org/10.4103/0974-2077.172206.

51. Karlsson, P., Nyengaard, J.R., Polydefkis, M., and Jensen, T.S. (2015). Structural and functional assessment of skin nerve fibres in small-fibre pathology. Eur. J. Pain *19*, 1059–1070. https://doi.org/10.1002/ejp.645.

52. Hsieh, S.T., Chiang, H.Y., and Lin, W.M. (2000). Pathology of nerve terminal degeneration in the skin. J. Neuropathol. Exp. Neurol. *59*, 297–307. https://doi.org/10.1093/jnen/59.4.297.

53. Yeh, H.Y., Lee, J.C., Chi, H.H., Chen, C.C., Liu, Q., and Yen, C.T. (2021). Longitudinal intravital imaging nerve degeneration and sprouting in the toes of spared nerve injured mice. J. Comp. Neurol. *529*, 3247–3264. https://doi.org/10.1002/cne.25162.

54. Alam, U., Jeziorska, M., Petropoulos, I.N., Asghar, O., Fadavi, H., Ponirakis, G., Marshall, A., Tavakoli, M., Boulton, A.J.M., Efron, N., and Malik, R.A. (2017). Diagnostic utility of corneal confocal microscopy and intraepidermal nerve fibre density in diabetic neuropathy. PLoS One *12*, e0180175. https://doi.org/10.1371/journal.pone.0180175.

55. Tavakoli, M., Petropoulos, I.N., and Malik, R.A. (2012). Assessing corneal nerve structure and function in diabetic neuropathy. Clin. Exp. Optom. *95*, 338–347. https://doi.org/10.1111/j.1444-0938.2012.00743.x.

56. Kalteniece, A., Ferdousi, M., Azmi, S., Mubita, W.M., Marshall, A., Lauria, G., Faber, C.G., Soran, H., and Malik, R.A. (2020). Corneal confocal microscopy detects small nerve fibre damage in patients with painful diabetic neuropathy. Sci. Rep. *10*, 3371. https://doi.org/10.1038/s41598-020-60422-7.

57. Petropoulos, I.N., Alam, U., Fadavi, H., Asghar, O., Green, P., Ponirakis, G., Marshall, A., Boulton, A.J.M., Tavakoli, M., and Malik, R.A. (2013). Corneal nerve loss detected with corneal confocal microscopy is symmetrical and related to the severity of diabetic polyneuropathy. Diabetes Care *36*, 3646–3651. https://doi.org/10.2337/dc13-0193.

58. Chen, X., Graham, J., Dabbah, M.A., Petropoulos, I.N., Ponirakis, G., Asghar, O., Alam, U., Marshall, A., Fadavi, H., Ferdousi, M., et al. (2015). Small nerve fiber quantification in the diagnosis of diabetic sensorimotor polyneuropathy: comparing corneal confocal microscopy with intraepidermal nerve fiber density. Diabetes Care *38*, 1138–1144. https://doi.org/10.2337/dc14-2422.

59. Ziegler, D., Papanas, N., Zhivov, A., Allgeier, S., Winter, K., Ziegler, I., Brüggemann, J., Strom, A., Peschel, S., Köhler, B., et al. (2014). German Diabetes Study (GDS) Group, Early detection of nerve fiber loss by corneal confocal microscopy and skin biopsy in recently diagnosed type 2 diabetes. Diabetes *63*, 2454–2463. https://doi.org/10.2337/db13-1819.

60. Chong, S.P., Merkle, C.W., Cooke, D.F., Zhang, T., Radhakrishnan, H., Krubitzer, L., and Srinivasan, V.J. (2015). Noninvasive, *in vivo* imaging of subcortical mouse brain regions with 1.7 μm optical coherence tomography. Opt. Lett. *40*, 4911–4914. https://doi.org/10.1364/OL.40.004911.

61. Yamanaka, M., Teranishi, T., Kawagoe, H., and Nishizawa, N. (2016). Optical coherence microscopy in 1700 nm spectral band for high-resolution label-free deep-tissue imaging. Sci. Rep. *6*, 31715. https://doi.org/10.1038/srep31715.

62. Matthews, T.P., Zhang, C., Yao, D.K., Maslov, K., and Wang, L.V. (2014). Label-free photoacoustic microscopy of peripheral nerves. J. Biomed. Opt. *19*, 16004. https://doi.org/10.1117/1.JBO.19.1.016004.

63. Xia, F., Wu, C., Sinefeld, D., Li, B., Qin, Y., and Xu, C. (2018). *In vivo* label-free confocal imaging of the deep mouse brain with long-wavelength illumination. Biomed. Opt Express *9*, 6545–6555. https://doi.org/10.1364/BOE.9.006545.

64. Jung, S.H., Kim, S., Chung, A.Y., Kim, H.T., So, J.H., Ryu, J., Park, H.C., and Kim, c.H. (2010). Visualization of myelination in GFP-transgenic zebrafish. Dev. Dynam. *239*, 592–597. https://doi.org/10.1002/dvdy.22166.

65. Shun, C.T., Chang, Y.C., Wu, H.P., Hsieh, S.C., Lin, W.M., Lin, Y.H., Tai, T.Y., and Hsieh, S.T. (2004). Skin denervation in type 2 diabetes: correlations with diabetic duration and functional impairments. Brain *127*, 1593–1605. https://doi.org/10.1093/brain/awh180.

66. Decosterd, I., and Woolf, C.J. (2000). Spared nerve injury: an animal model of persistent peripheral neuropathic pain. Pain *87*, 149–158. https://doi.org/10.1016/S0304-3959(00)00276-1.

67. Bourquin, A.F., Süveges, M., Pertin, M., Gilliard, N., Sardy, S., Davison, A.C., Spahn, D.R., and Decosterd, I. (2006). Assessment and analysis of mechanical allodynia-like behavior induced by spared nerve injury (SNI) in the mouse. Pain *122*, 14.e1, 14e14. https://doi.org/10.1016/j.pain.2005.10.036.

68. Anderson, R.R., and Parrish, J.A. (1981). The optics of human skin. J. Invest. Dermatol. *77*, 13–19. https://doi.org/10.1111/1523-1747.ep12479191.

69. Wu, P.-J., Chen, S.-T., Liao, Y.-H., and Sun, C.-K. (2021). *In vivo* harmonic generation microscopy for monitoring the height of basal keratinocytes in solar lentigines after laser depigmentation treatment. Biomed. Opt Express *12*, 6129–6142. https://doi.org/10.1364/BOE.434789.

70. Sun, C.K., Wu, P.J., Chen, S.T., Su, Y.H., Wei, M.L., Wang, C.Y., Gao, H.C., Sung, K.B., and Liao, Y.H. (2020). Slide-free clinical imaging of melanin with absolute quantities using label-free third-harmonic-generation enhancement-ratio microscopy. Biomed. Opt Express *11*, 3009–3024. https://doi.org/10.1364/BOE.391451.

71. Sun, C.-K., Liu, W.-M., and Liao, Y.-H. (2019). Study on melanin enhanced third harmonic generation in a live cell model. Biomed. Opt Express *10*, 5716–5723.

72. Wu, P.-J., Chen, S.-T., Sheen, Y.-S., Sun, C.-K., and Liao, Y.-H. (2022). A longitudinal comparative study by *in vivo* harmonic generation microscopy: Q-switched ruby laser versus picosecond 532-nm Nd: YAG laser

for the treatment of solar lentigines. JEADV Clin. Pract. *1*, 372–382. https://doi.org/10.1002/jvc2.57.

73. Liao, Y.-H., Su, Y.-H., Shih, Y.-T., Chen, W.-S., Jee, S.-H., and Sun, C.-K. (2019). *In vivo* third-harmonic generation microscopy study on vitiligo patients. J. Biomed. Opt. *25*, 1–13. https://doi.org/10.1117/1.JBO.25.1.014504.

74. Wang, L., Hilliges, M., Jernberg, T., Wiegleb-Edström, D., and Johansson, O. (1990). Protein gene product 9.5-immunoreactive nerve fibres and cells in human skin. Cell Tissue Res. *261*, 25–33. https://doi.org/10.1007/BF00329435.

75. Hilliges, M., Wang, L., and Johansson, O. (1995). Ultrastructural evidence for nerve fibers within all vital layers of the human epidermis. J. Invest. Dermatol. *104*, 134–137. https://doi.org/10.1111/1523-1747.ep12613631.

76. Lin, K.-H., Liao, Y.-H., Wei, M.-L., and Sun, C.-K. (2020). Comparative analysis of intrinsic skin aging between Caucasian and Asian subjects by slide-free *in vivo* harmonic generation microscopy. J. Biophot. *13*, e201960063. https://doi.org/10.1002/jbio.201960063.

## STAR★METHODS

### KEY RESOURCES TABLE

| REAGENT or RESOURCE | SOURCE | IDENTIFIER |
|---|---|---|
| Antibodies | | |
| Anti-PGP9.5 primary antibody | Abcam, Inc., Cambridge, UK | Cat # ab108986 |
| Biotinylated goat antirabbit immunoglobulin G | Vector, Burlingame, CA, USA | Cat # BA-1000 |
| DyLight-488 anti-rabbit IgG | Vector, Burlingame, CA, USA | Cat # DI-1088 |
| Biological samples | | |
| Healthy human adult sole skin tissue | This paper | National Taiwan University Hospital (No. 201610037DINC) |
| Chemicals, peptides, and recombinant proteins | | |
| Potassuim Permanganate | Kanto chemical co., Inc.,Japan | Cat # 32373-00 |
| Oxalic acid dihydrate | Kanto chemical co., Inc.,Japan | Cat # 31045-01 |
| Hydrogen Peroxide | Kanto chemical co., Inc.,Japan | Cat # 18084-00 |
| Triton X-100 | Sigma-Aldrich Co, USA | Cat # SLBN8333V |
| Trizma(R) base | Sigma-Aldrich Co, USA | Cat # SLBV9322 |
| Methanol | Sigma-Aldrich Co, USA | Cat # SZBG0150V |
| Critical commercial assays | | |
| Avidin-biotin complex kit | Vector, Burlingame, CA, USA | Cat # PK-6100 |
| Chromogen SG | Vector, Burlingame, CA, USA | Cat # SK-4700 |
| Experimental models: Organisms/strains | | |
| Mouse: C57BL/6J | The Jackson Laboratory | Stock #000664 |
| Software and algorithms | | |
| ImageJ | National Institutes of Health, USA | https://imagej.net/ij/ |
| MATLAB | MathWorks, USA | https://www.mathworks.com/ |
| ThorImage®LS | Thorlabs, Inc. | https://www.thorlabs.com/ |
| Leica ICC50D | Leica Microsystems Inc. | https://www.leica-microsystems.com/ |
| SPSS software | IBM Corporation, Armonk, NY, USA | https://www.ibm.com/products/spss-statistics |
| Other | | |
| iSpacer | SunJin Lab Co. | Cat # ISO11 |

### RESOURCE AVAILABILITY

#### Lead contact

Further information and requests for resources and reagents should be directed to and will be fulfilled by the lead contact, Prof. Chi-Kuang Sun (sun@ntu.edu.tw).

#### Materials availability

This study did not generate new unique reagents.

#### Data and code availability

- For the small-animal experiments, the data supporting the findings of this study are available from the lead contact upon reasonable request. For the clinical trials, the data are only available to researchers engaged in the IRB-approved research collaborations from the author upon a reasonable request. These data are not publicly available to other research because they contain information that could compromise privacy or consent. The corresponding author (W.-Z. Sun) can, however, consider specific requests on a case-by-case basis.
- This paper does not report original code.
- Any additional information required to reanalyze the data reported in this work paper is available from the lead contact upon request.

## EXPERIMENTAL MODEL AND STUDY PARTICIPANT DETAILS

### Mice model

Three wild-type C57BL/6J Narl mice used in this study were 8–16 weeks old. All mice with an average weight of 25 g and were housed under a 12-h light–dark cycle at a temperature of 22°C, with food and water provided *ad libitum*. Both male and female mice were used in this study. All animal care and experimental procedures were approved by the Institutional Animal Care and Use Committee of National Taiwan University (approval number: NTU107-EL-00176).

### Human sole skin sample and study volunteers

For *in vivo* human study, three female patients aged 62–70 years (mean age: 67 ± 4.36 years) who had received a clinically diagnosis of DPN were recruited. We also recruited 11 individuals (3 men and 8 women) aged 24–62 years (mean: 35.18 ± 13.36 years) who were confirmed to be without diabetes or neuropathy on the basis of glycated hemoglobin (HbA1C) blood test reports and neurological examinations as controls. The study protocol was approved by the Research Ethics Committee of National Taiwan University Hospital (No. 201610037DINC) and the Taiwan Food and Drug Administration. Written informed consent was provided by all patients before the experiment. This trial was conducted in accordance with the principles of the Declaration of Helsinki. *In vivo* dTHGM imaging was performed at the Molecular Imaging Center of National Taiwan University. For human *ex vivo* study, human sole skin tissues collected from the lower distal extremities of three individuals. The study protocol was approved by the Research Ethics Committee of National Taiwan University Hospital (No. 200903064D), and informed consent was provided by all patients before study entry.

## METHOD DETAILS

### IHC staining of human skin sections for *ex vivo* study

The sole skin tissue of the human foot was cryoprotected with 30% sucrose and continually sectioned (thickness: 50 μm) using a cryostat (Leica CM 1950, Leica Biosystems, Wetzlar, Germany) for a total duration of 1 h. For each sole skin section, the areas suspected to have FINE-like signals at the epidermis or DEJ were imaged, and the acquisition position was recorded immediately.

It is noted that the skin nerve biopsy frequently proceeded on the distal part of the lower leg, more specifically, 10 cm above the external malleolus. Most of the studies sustain the same biopsy site because of the IENFDs could vary according to the location. Here we choose sole, which is part of foot and is different from the regular biopsy site, due to several reasons. First is due to its availability under the specific study protocol. Second, the study protocol was limited to the comparison between the contrast of IHC staining imaging and contrast of dTHGM imaging, which is not considered site dependent. Results are shown in Figures 2, 3, and 4. This study protocol did not involve IENFD comparison. Third, we prefer foot skin, which could also be considered on the lower extremity, due to its low melanin content for possible dTHGM imaging. It is further noted that for the comparison of quantified results of intraepidermal nerve fiber densities between biopsy-obtained IENFD and IENF index (as shown in Figure 6), the skin biopsies for the three patients with DPN proceeded on the distal part of the lower leg, 10 cm above the external malleolus.

After *ex vivo* TFETM imaging for a total of 15 min, human skin sections were immediately subjected to IHC staining with PGP9.5, in accordance with the procedure described in a previous study.[65] The skin sections were fixed with 4% paraformaldehyde for 6 h, treated with 0.1 M phosphate buffer (PB; pH 7.4), and then stored for 12 h. Furthermore, the skin sections were quenched with 1% $H_2O_2$, blocked with 5% normal goat serum, and incubated with rabbit antiserum to PGP9.5 (Abcam, Cambridge, UK, diluted 1:500 in 1% normal serum/Tris) at 4°C for 16–18 h. The sections were rinsed in Tris, followed by incubation with the avidin-biotin complex (Vector, Burlingame, CA, USA) for 40 min. The sections were then incubated with biotinylated goat antirabbit immunoglobulin G at room temperature for 1 h. The reaction product was visualized using chromogen SG (Vector). PGP9.5-immunoreactive nerve fibers present in the epidermis of each section were counted under a light microscope at a magnification of 40× (Leica ICC50D, Leica, Germany).

### Small-animal model of SNI

The mice were anesthetized using ketamine (50 mg/kg) and xylazine (15 mg/kg). SNI surgery was performed in accordance with the procedures described by Decoster and Woolf and by Burqini et al.[66,67] Briefly, the fur on the left thigh was shaved. The skin and muscle near the knee were incised, and the left sciatic nerve was exposed. The common peroneal and tibial nerves—the two main branches of the sciatic nerve—were tightly ligated using a 6/0 silk suture, and a section of each of the two nerves was excised using corneal scissors. The sural nerve was left intact. The muscle and skin were then sutured using 6/0 silk. Lincomycin hydrochloride (30 mg/kg) was administered into the right gastrocnemius muscle to prevent infection. For the observation of epidermal innervation on the third toe using dTHGM, we recorded the acquisition positions at baseline and at 24 and 48 h after SNI surgery.

### Tightly focused epi-THG microscopy (TFETM)

In the TFETM system, laser pumping is performed using a femtosecond Cr:forsterite laser with a repetition rate of 105 MHz, bandwidth of 91 nm, and central wavelength of 1262 nm; this wavelength is not only located within the transmission window

of human skin but also avoids melanin absorption and has low skin scattering.[68] Therefore, its optical penetration depth can reach the DEJ, even in the human distal skin or glabrous skin. Double-chirped mirrors are applied to control the optical dispersion. The laser beam is collimated and guided with a light guide (1.25 Series Laser Articulated Arms; LaserMech, Novi, Michigan, USA) into galvoresonant mirrors (Laser Scanning Essentials Kit; Thorlabs, Newton, NJ, USA) to perform 2D scanning. To achieve a tightly focused Gaussian beam, a 1.15-NA objective (40×; working distance: 250 μm; UApo N 340; Olympus, Tokyo, Japan) is used to focus the laser beam onto the skin. Both the backpropagated THG (∼420 nm) and the SHG (∼630 nm) signals are collected using the same objective and are separately detected by two photomultiplier tubes (R928 for epi-SHG and R4220P for epi-THG; Hamamatsu Photonics, Hamamatsu City, Japan). Band-pass filters with different center wavelengths and bandwidths (FF02-617/73 for epi-SHG and FF01-417/60 for epi-THG, Semrock) are inserted before the photomultiplier tubes (PMTs) to filter out the background noise and increase the signal-to-noise ratio. The objective is attached to a 3D step motor (TSDM40-15X, Sigma Koki, Japan) such that the 3D position of the objective can be adjusted both manually and with electrical controls. The depth of the imaging plane is controlled by tuning the 3D stage along the optical axis. Similar to the pulse width measurement and dispersion control method described in a previous study,[69] the pulse width after the objective is approximately 28 fs. Moreover, the epi-THG transverse and axial resolutions are approximately 0.4 and 1.3 μm, respectively.[70]

### Sample preparation for postfixation IHC staining

To avoid the effects of the fixation solution (4% paraformaldehyde) and IHC staining on the epi-THG signal for histological validation, postfixation staining was necessary. A fresh human skin section was cryoprotected with 30% sucrose, followed by frozen section fixation. The total duration required was 1 h. We performed postfixation IHC staining 15, 30, and 60 min after completing the TFETM imaging (resulting in a cumulative delay of 1.25, 1.5, and 2 h, respectively, for postfixation staining). The IHC staining study revealed that the FINEs degenerated completely after a 1.5-h delay in postfixation staining. After 2 h of delay, the individual nerve fibers in the dermal nerve trunks either disappeared or exhibited fragmented immunoreactivity, indicating the complete degeneration of nerve fibers. These results indicate that *ex vivo* dTHGM imaging for histological validation should be completed within 15 min after frozen section preparation and that FINE degeneration should be expected.

### Imaging procedure

All of the 3D THG image stacks (14-bit grayscale) comprised a series of 2D *en face* images (512 × 512 pixels; field of view [FOV], 235 × 235 μm). The acquisition time was approximately 0.38 s per averaged image collected by averaging five frames at a fixed depth with a 15-Hz frame rate. *Ex vivo* and *in vivo* THG images were acquired at different depths from the surface every 0.6 and 1.8 μm along the optical axis, respectively.

### Imaging acquisition area selection for clinical *in vivo* dTHGM imaging

According to previous studies, the THG intensity is sensitive to melanin, whereas the melanin mass density of the focal volume is directly related to the intensity of the THG signal in the basal layer.[39,70–73] In this study, although the THG signal was also found to be highly sensitive to the presence of FINEs, the nerve fibers were mostly distributed among the basal keratinocytes, causing them to be easily shadowed by the surrounding background THG from melanin. For patients with diabetic neuropathy, the most common site of symptoms is the distal extremities and with a length-dependent process; thus, areas with a low melanin content on the distal leg are excellent candidate sites for dTHGM. Figures 7 A–7F depicts the TFETM images acquired in candidate areas on the terminal of the distal leg, including the sole, heel, instep arch, bridge, and ankle (Figure 7G). For positions 1, 2, 5, and 6, the high melanin content in the basal layers provided a strong THG background. By contrast, positions 3 and 4 had little melanin in their basal layers. Accordingly, we concluded that the instep arch was the optimal choice for dTHGM. Moreover, the excessively thick stratum corneum (SC) of the sole and heel of the foot caused substantial light scattering; hence, an objective with a longer working distance was required.

### *In vivo* dTHGM of the lower distal extremities

All *in vivo* dTHGM image stacks were acquired using the same imaging conditions, and at least 20 3D image stacks were acquired for each participant from the instep arch of the lower distal extremities. The average laser power after the objective was 105 mW, and the voltages of the PMTs for the epi-SHG and epi-THG modalities were set at 700 and 800 V, respectively. Each 3D image stack comprised 150 depth-dependent 2D subimages with two channels, which were obtained through the skin surface and upper dermis. We selected 1.8 μm as the *z*-step size for the optical section. To ensure a 250-μm-depth stack, 150 steps were acquired (at the 1.8-μm step size) over a total of 55 s. An objective adaptor with a medical tape (3M Double Coated Medical Tape No. 9874) was used to fix and stabilize the relative position of the imaged skin to avoid motion artifacts. The allowed acquisition time for one participant was <40 min. Therefore, the total laser energy accumulated in the same area was <200 J. We conducted our photodamage examination under similar clinical conditions to those described in a previous study[73]; the evaluation results obtained in this study were noted to be the same as those in the aforementioned study. Specifically, we observed no erythema, pigmentation, or blister formation on the examined skin.

## QUANTIFICATION AND STATISTICAL ANALYSIS

### Discontinuous-dot-connecting algorithm

A discontinuous-dot-connecting algorithm was developed to identify the FINEs and count the number of IENFs within the TFETM imaging area. The operating flow (Figure 7I) of the algorithm is summarized as follows:

***Step 1:*** According to,[74] the FINEs are distributed throughout the stratum basal and stratum spinosum and terminate at the stratum granulosum. Thus, the subimages of the TFETM image stack from the stratum granulosum layer to the dermis (D) were analyzed. The SC layer is a thick layer of dead skin cells, and the stratum lucidum (SL) layer is a thin layer of dead skin cells that can only be seen on the palms and soles of the feet. No FINEs are distributed in the SC and the SL layers.[75] The definitions of the skin layer in the TFETM image are as described in a previous study.[76]

***Step 2:*** Each single-layer image from the stratum granulosum to D layers was analyzed. We observed that FINE signals appeared as dot-like and bead-like patterns. Because the literature reveals that the axon diameter of unmyelinated FINEs ranges from 0.2 to 1.5 μm, as determined through electron micrography (Introduction), the size of dot-like dTHG signal patterns should be greater than 200 nm. Bead-string-like patterns are produced by dTHG signals comprising dense dot-like patterns extending in one or multiple orientations. If the dTHG signal of a single-layer image is a bead-string-like pattern, Step 4 of the protocol was executed, skipping Step 3.

***Step 3:*** Our IHC staining revealed that the interval distance between varicosity structures of unmyelinated FINEs was 1.28–10.4 μm (see the results section for more details). In this step, we considered images at different layers of the TFETM image stack. If the dot-like dTHG signal pattern extended along the same or multiple directions in images at different layers, the pattern could indicate a FINE if the signal was consecutive; that is, the distance between dot-like signals was less than 10.4 μm. Otherwise, the signal was excluded.

***Step 4:*** Three conditions were considered in this step. First, circular signals resembling cell contours were excluded. Second, to avoid mistaking FINEs for melanocyte dendrites, we excluded dendritic-cell-like THG signals. Third, dTHG traces with fewer than five consecutive dot-like signals were excluded. Consecutive signals have interdot distances of less than 10.4μm.

***Step 5:*** As shown in cases E and F in Figure 7H, if one FINE signal fragment is distributed in the upper epidermis (in stratum spinosum and stratum granulosum) and another is distributed near the DEJ, these two fragments may belong to the same nerve fiber. If only one FINE fragment is located in the upper epidermis, the nerves close to the DEJ may be distributed outside the stack due to the limited FOV. To avoid double counting, we considered the distance between the FINE signal in the epidermis and the DEJ. If the closest distance between the FINE signal and the DEJ is less than 5 μm, the FINE structure inside the epidermis was counted as one IENF.

### Quantification of the IENF index

The IENF index corresponds to the IENF area density. However, it differs from the density in that the IENF density of a skin biopsy is one-dimensional, whereas the IENF index is calculated for an area.

$$\text{IENF index}\left(\frac{\text{fibers}}{\text{mm}^2}\right) = \frac{\text{number of IENF (fibers)}}{\text{examined skin area (mm}^2\text{)}}$$

The examined skin area is equivalent to the total horizontal microscope FOV parallel to the skin surface. Each IENF in an image stack with branching points in the epidermis can be considered to be one unit, and each IENF with branching points in the dermis can be counted separately. Accordingly, the IENF index can be derived (fibers/mm$^2$). To ensure that the obtained nerve density is representative, the total FOV area must be > 1 mm$^2$ for each subject. We conducted two inspection procedures to ensure that all *in vivo* 3D image stacks with any longitudinal or lateral motion artifacts in the imaged epidermis were excluded as invalid. Specifically, a preliminary inspection was performed immediately after the acquisition of the THG images. If an obvious motion blur was detected, the image stack was excluded, and the microscopy images were reacquired. Subsequently, a second inspection was performed while analyzing the clinical data; images with lateral or axial motion artifacts in the epidermis were recorded and excluded.

### IENF index calibration

Because people's skin conditions differ, a calibration factor, which may affect the THG intensity, should be selected for the IENF index. Moreover, lower THG intensities at the DEJ layer caused by the greater epidermal thickness result in a lower signal-to-background ratio for FINEs signals. Owing to the lack of other data and information about the relationship between nerves and the calibration factor, we made the simplest assumption that the relationship between the calibration factor and the IENF index should be linear. Accordingly, the IENF index was linearly calibrated according to this factor. We considered the epidermal thickness to be the calibration factor.

### Statistical analysis

All collected data were decoded and analyzed by blinded evaluators using SPSS software (version 20.0; IBM Corporation, Armonk, NY, USA). A two-sided Student's *t* test was conducted for data analysis. p values of <0.05 denoted statistically significant differences. Pearson correlation analysis was performed to measure the strength of the linear relationship between the two variables (IENF density and IENF index) in this study.